

Polyfluorene Derivatives are High-Performance Organic Hole-Transporting Materials for Inorganic–Organic Hybrid Perovskite Solar Cells

Zonglong Zhu, Yang Bai, Harrison Ka Hin Lee, Cheng Mu, Teng Zhang, Lixia Zhang, Jiannong Wang, He Yan, Shu Kong So, and Shihe Yang*

Photovoltaics based on organic–inorganic perovskites offer new promise to address the contemporary energy and environmental issues. These solar cells have so far largely relied on small-molecule hole transport materials such as spiro-OMeTAD, which commonly suffer from high cost and low mobility. In principle, polyfluorene copolymers can be an ideal alternative to spiro-OMeTAD, given their low price, high hole mobility and good processability, but this potential has not been explored. Herein, polyfluorene derived polymers-TFB and PFB, which contain fluorine and arylamine groups, are demonstrated and can indeed rival or even outperform spiro-OMeTAD as efficient hole-conducting materials for perovskite solar cells. In particular, under the one-step perovskite deposition condition, TFB achieves a 10.92% power conversion efficiency that is considerably higher than that with spiro-OMeTAD (9.78%), while using the two-step perovskite deposition method, about 13% efficient solar cells with TFB (12.80%) and spiro-OMeTAD (13.58%) are delivered. Photoluminescence reveals the efficient hole extraction and diffusion at the interface between $\text{CH}_3\text{NH}_3\text{PbI}_3$ and the hole conducting polymer. Impedance spectroscopy uncovers the higher electrical conductivity and lower series resistance than spiro-OMeTAD, accounting for the significantly higher fill factor, photocurrent and open-circuit voltage of the TFB-derived cells than with spiro-MeOTAD.

1. Introduction

Solar energy is a clean and inexhaustible natural resource.^[1] Photovoltaic (PV) solar cells are devices that make direct conversion of solar photons into electricity.^[2] At the present-day,

crystalline silicon solar cells^[3] and other thin film vapor-phase deposited semiconductor-based solar cells,^[4] which are often referred to as the first- and the second- generation of PVs, make up most of the commercial market shares. The third-generation of PVs, which leverage new concepts such as tandem structure,^[5] hot carrier extraction,^[6] multiple exciton generation^[7], multiband design^[8] and thermo-PVs,^[9] are widely considered as more cost-effective, reliable and sustainable energy sources, and have become the pivot of scientific and technological pursuits for the past two decades.

Recently, an unexpected breakthrough of perovskite-typed solar cell has piqued high attention and opened up a new vista in the PV field.^[10] The earliest use of the perovskite sensitizer ($\text{CH}_3\text{NH}_3\text{PbX}_3$, X is halogen) was partnered with the infusion of a liquid electrolyte into a TiO_2 mesoporous film, resulting in a 3.8% PV efficiency with lack of stability.^[11] In a dramatic development, the groups of

Park,^[12] Snaith^[13] and Gratzel^[14] replaced the liquid electrolyte by a hole transport layer (HTL) of 2,2',7,7'-tetrakis(*N,N*-dimethoxyphenylamine)-9,9'-spirobifluorene (spiro-OMeTAD), the cell efficiency was rapidly improved. The latest power conversion efficiency (PCE) has reached more than 15% for both mesoporous and planar cell architectures.^[13–15] Although spiro-OMeTAD as a small molecule hole conductor has been a game changer for the perovskite solar cells,^[16] it suffers from the low mobility (about 10^{-6} – 10^{-5} cm^2/Vs)^[17] in its pristine form. It is known that the hole conductivity was increased by over an order of magnitude after doping with cobalt electrolyte and lithium salts,^[18] but it remains an efficiency limiting factor of perovskite solar cells.^[10a] Recently, other small molecule hole transporters have also been reported based on derivatives of pyrene^[19] and thiophene.^[20] However, the small molecules, including spiro-OMeTAD, are often expensive, involve multistep synthesis, and are difficult for device fabrication, limiting their potential applications in commercial photovoltaics. In parallel, even inorganic materials were used as the HTL,^[21] but the efficiency remains low due to the low open-circuit voltage.

For perovskite solar cells, hole conducting polymers (HCPs) are advantageous for their low cost, processability, accessibility

Z. L. Zhu, T. Zhang, S. H. Yang
Nano Science and Technology Program
The Hong Kong University of Science and Technology
Clear Water Bay, Kowloon, Hong Kong
E-mail: chsyang@ust.hk

Z. L. Zhu, Y. Bai, C. Mu, T. Zhang, H. Yan, S. H. Yang
Department of Chemistry
The Hong Kong University of Science and Technology
Clear Water Bay, Kowloon, Hong Kong
L. X. Zhang, J. N. Wang
Department of Physics
The Hong Kong University of Science and Technology
Clear Water Bay, Kowloon, Hong Kong

H. K. H. Lee, S. K. So
Department of Physics
Hong Kong Baptist University
Kowloon, Hong Kong

DOI: 10.1002/adfm.201401557



and large choice. Indeed, arylamine derived conjugated polymers were explored as hole transporting and electron blocking layers. The highest efficiency achieved was 16.2% with PTAA^[22] in meso-superstructured perovskite solar cells and over 12% and 10% with poly-TPD and P3HT^[23] in planar thin film perovskite solar cells. These results demonstrated that the performances of the perovskite solar cells based on the HCPs compare favorably with those based on the small molecule spiro-OMeTAD.

In the burgeoning field of perovskite solar cells, it is of paramount importance to expand the family of the HCPs for efficient hole extraction and transport. Principal considerations for choosing HCPs generally include high hole mobility, dopability, tunable energy of the highest occupied molecular orbital (HOMO), which need match well with the VB of perovskite to enable hole extraction and electron blocking, as well as high processability and stability. Polyfluorenes (PFs) are a class of polymeric materials which contain the structure of fluorine groups, and being widely used in light emitting diodes, field effect transistors, and polymer solar cells.^[24] In this study, by introducing the electron-rich *N*-triphenyl groups in the monomer units to tune the energy levels, we establish a family of superior HTMs for CH₃NH₃PbI₃ perovskite-sensitized solar cells. Toward this end, TFB is used as an archetype of fluorene-*N*-triphenyl based polymers to serve as the hole-transport layer. We have studied the hole-transporter based solar cells under both two-step and one-step perovskite deposition conditions. Promisingly, under the more general one-step perovskite deposition condition, TFB shows a remarkable cell performance with a significantly higher PCE (over 10.92%) than spiro-OMeTAD (9.78%) under AM 1.5 G one-sun illumination. To understand the origin of the excellent cell performance of TFB, two analogues of TFB, PFB and PFO, were comparatively studied, which yielded PCEs of 8.03% and 1.22%, respectively. It was found that the hole mobility and the energy levels are very sensitive to the structures of the building blocks of the polymers, leading to the largely varied performance of the corresponding solar cells. Dynamic photoluminescence and impedance spectroscopy has been employed to tap into the detailed correlation between the material electronic parameters of HCPs, including hole mobility, energy level alignments, etc., and the cell performance metrics, such as open-circuit voltage, short-circuit photocurrent and fill factor. Parenthetically, we also tested the two-step CH₃NH₃PbI₃ deposition method and achieved a PCE up to 12.80% when using TFB as HTM and 13.58% with spiro-OMeTAD, which are fairly comparable and thus attest the competency of TFB for perovskite solar cells.

2. Results and Discussion

2.1. Optical, Electronic, and Electric Characterizations of HCPs

The derived polyfluorene polymers used here are Poly(9,9-dioctylfluorenyl-2,7-diyl) (PFO), poly [(9,9-dioctylfluorenyl-2,7-diyl)-co-(4,4'-(*N*-(4-sec-butylphenyl)diphenylamine)] (TFB) and poly(9,9-dioctylfluorene-co-bis-*N*,*N*-(4-butylphenyl)-bis-*N*,*N*-phenyl-1,4-phenylenediamine) (PFB). The chemical structures are shown in Figure 1. Figure 2B confirms the high

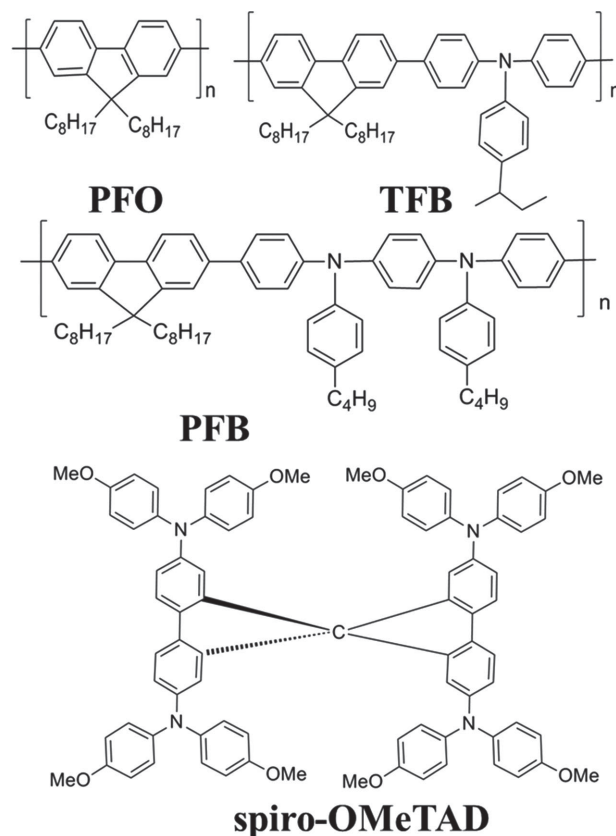


Figure 1. Chemical structures of the hole-transporting layer materials: PFO, TFB, PFB, spiro-OMeTAD.

transparency of the polymer thin films on transparent conducting glass substrates (FTO), and therefore the polymers would not compete for light absorption with the perovskite.

Figure 2A schematizes the relevant energy levels, the highest occupied molecular orbital (HOMO) and the lowest unoccupied molecular orbital (LUMO), of the PFs and the reference small molecule spiro-OMeTAD, together with those of the electron injection targets perovskite and TiO₂. The HOMO and LUMO positions of the HCPs are also listed in Table 1. PFO is a homopolymer of fluorene, and its HOMO is located at −5.8 eV, which is below the VB of CH₃NH₃PbI₃ and thus would make PFO a poor hole extractor for perovskite solar cells as was reported previously.^[25] For TFB and PFB, the monomeric blocks contain, apart from the one fluorene unit, one and two arylamine groups, respectively. The arylamine group is an electron donor and raises the energy levels of the HCPs. For example, TFB has a HOMO level of −5.3 eV and LUMO level of −1.9 eV with respect to the vacuum energy, which we find matches rather well with the VB (−5.4 eV) of CH₃NH₃PbI₃.^[26] The HOMO and LUMO of PFB have been pushed up even further, which could help hole extraction but may compromise other advantages such as photovoltage. Therefore, compared with PFO, PFB and spiro-OMeTAD, TFB appears to have the best combination of the HOMO and LUMO energy levels, which would allow it to efficiently extract holes and block electrons while maintaining a high photovoltage at the same time.

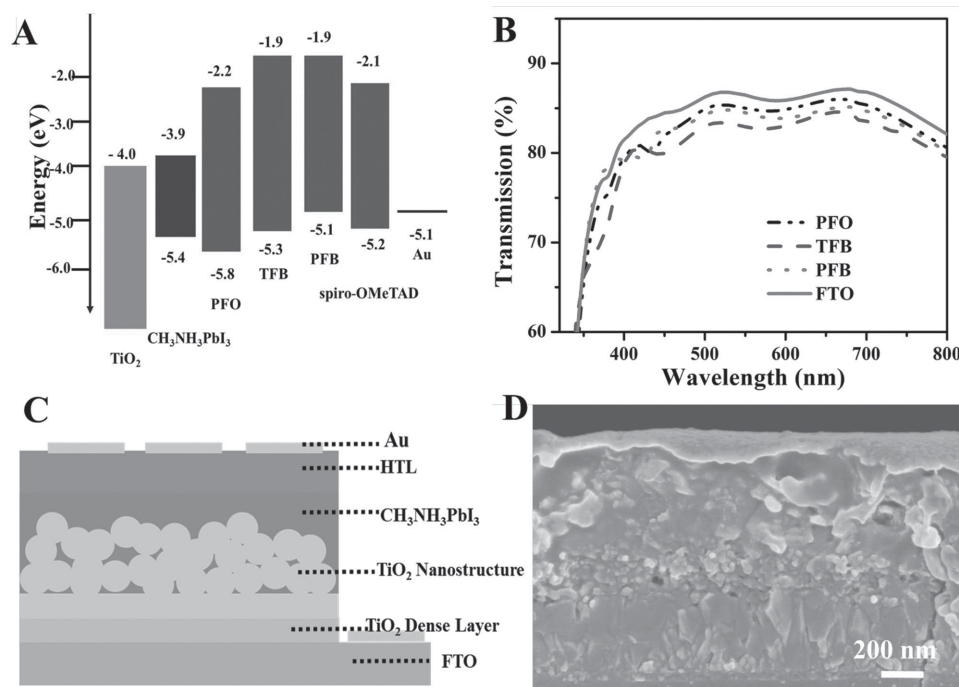


Figure 2. A) Energy band diagram and B) absorption spectra of thin film of PFO (dash dot dot line), TFB (dash line) and PFB (dot line), and FTO blank (solid line). C) Schematic representation and cross-sectional SEM image of the photovoltaic device structure used the TiO_2 nanostructure thin film with different hole-transporting layer (HTL). D) Cross-sectional SEM image of a typical photovoltaic device. Note that the thin TiO_2 layer present between the FTO and $\text{CH}_3\text{NH}_3\text{PbI}_3$ is not resolved in the SEM image.

As for hole mobility, which has also been collected in Table 1 for the materials of interest in this work, the HCPs are generally superior to spiro-OMeTAD ($2 \times 10^{-5} \text{ cm}^2/\text{Vs}$)^[17]. In particular, the hole mobility of TFB ($1 \times 10^{-2} \text{ cm}^2/\text{Vs}$)^[27] is higher than that of spiro-OMeTAD by as much as over 3 orders of magnitude, while PFB and PFO also have appreciably higher hole mobility of $3 \times 10^{-4} \text{ cm}^2/\text{Vs}$ and $1.5 \times 10^{-4} \text{ cm}^2/\text{Vs}$, respectively.^[28]

2.2. Photovoltaic Cell Assembly with HCPs

To gauge the performance of the HCPs in real devices, perovskite ($\text{CH}_3\text{NH}_3\text{PbI}_3$) solar cells were fabricated utilizing PFO, PFB and TFB as the hole-transporting materials, and a reference cell using spiro-OMeTAD was also assembled for comparison (see Experiment Section for details). Both the two-step and one-step perovskite deposition conditions were tested. However, due to its more general applicability, the one-step condition was adopted for thorough and systematic studies to be presented below. In fact, extensive two-step deposited PV

results are also presented in Supporting Information. In a typical one-step deposition process, a mesoporous TiO_2 nanocrystals layer with a thickness of $\approx 300 \text{ nm}$ was spin-coated onto a pre-deposited TiO_2 dense layer on FTO. This was followed by spin-coating first a thin absorber layer of organometal halide perovskite ($\text{CH}_3\text{NH}_3\text{PbI}_3$) and then a HCP layer. Figure 2C,D shows, respectively, a schematic representation and a SEM image of a complete solar cell in cross-sectional view; in this PV device structure, TFB was used as the HTM. The total thickness of the solar cell is about 680 nm , consisting of the 30 nm TiO_2 dense layer, the 550 nm layer of TiO_2 nanocrystals imbued with perovskite $\text{CH}_3\text{NH}_3\text{PbI}_3$, and the final uniformly capped HCP layer (100 nm TFB film).

We also examined the influence of the HTL thickness of TFB on the surface morphology (see Figure S1, Supporting Information). The HTL thickness was controlled by varying the concentration in chlorobenzene. During the perovskite deposition, $\text{CH}_3\text{NH}_3\text{PbI}_3$ pillars or islands are usually formed on top of the TiO_2 film.^[29] Thus when the HTL is thin, some of the surface is not covered with HTMs as shown in Figure S1A.

Table 1. The energy level of HOMO and LUMO, hole mobility, and quenching efficiency of different HTMs with $\text{CH}_3\text{NH}_3\text{PbI}_3$ perovskite.

Hole transport materials	HOMO [eV]	LUMO [eV]	μ_{hole} at $\approx 90 \text{ kV/cm}$ at $\approx \text{RT}$ (cm^2/Vs)	$\eta_{\text{quenching}}$
PFB ^[28b]	-5.1	-1.9	3×10^{-4}	0.86
TFB ^[26,27]	-5.3	-1.9	1×10^{-2} , 7×10^{-3}	0.91
PFO ^[25,28a]	-5.8	-2.2	1.5×10^{-4} , 1.3×10^{-5}	0.22
Spiro-OMeTAD ^[17]	-5.1	-2.1	2×10^{-5}	0.94

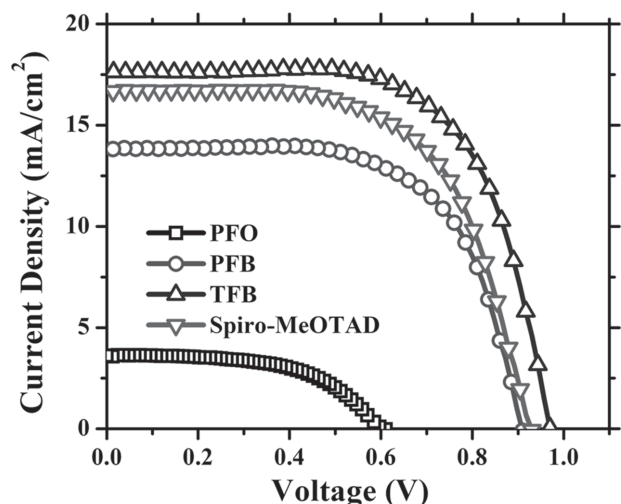


Figure 3. Current density–voltage curves for the best-performing solar cells with different HTL under AM 1.5 G illumination at 100 mW/cm². PFO (square line), PFB (circle line), TFB (up triangle line), Spiro-MeOTAD (down triangle line).

With increasing thickness of TFB to 100 nm, the CH₃NH₃PbI₃/TiO₂ film becomes fully covered, and we found that the TFB could also be infiltrated into the mesopores wherever present on the surface (see Figure S1B). But when the thickness is increased to 150 nm (Figure S1C), even the highest pinnacles of the CH₃NH₃PbI₃/TiO₂ film are covered up to 100 nm (Figure S1C). Finally, when the thickness is increased to 300 nm, the CH₃NH₃PbI₃ surface is flattened as all the pillars and islands are buried in the overlayer of TFB. These HTL thickness effects are quite consequential to the PV device performance, and the relative discussions will be given below.

2.3. Photovoltaic Performance

Figure 2A presents the energy level alignment diagram of device based on different HTL or electron blocking materials. The valence band (VB) and conduction band (CB) of the CH₃NH₃PbI₃ perovskite are −5.4 and −3.9 eV, relative to the vacuum level. The photoelectrons would transfer to the CB of the TiO₂ layer and the photoholes would move to the HOMO of the HTL when free excitons are generated in the perovskite CH₃NH₃PbI₃ absorber layer.

Shown in Figure 3A are photocurrent density–voltage (*J*–*V*) curves for the cells fabricated using PFO, PFB, and TFB of HTMs. The device performance parameters are summarized in Table 1. For meaningful comparisons, we also fabricated the PV devices without HTL as well as with different thicknesses of Spiro-OMeTAD. Impressively, the TFB based device with the optimized thickness displays a PCE 10.92% with a short-circuit current density (*J*_{SC}) 17.5 mA/cm², open circuit voltage (*V*_{OC}) 0.96 V, and fill factor (FF) 0.65, while with PFB, a lower PCE of 8.03% (*J*_{SC} 13.8 mA/cm², *V*_{OC} 0.91 V, and FF 0.64) was obtained. In contrast, the PFO-based cell exhibits a very low PCE of 1.22% with *J*_{SC} 3.6 mA/cm², *V*_{OC} 0.61 V, and FF 0.56, even lower than that of the cell without HTMs. This can be explained by the low HOMO position of PFO (−5.8 eV),

which made the hole extraction ineffective from the VB level of the CH₃NH₃PbI₃ absorber (−5.4 eV). Much to our delight, compared with the Spiro-OMeTAD based cell, which acquires a 9.78% PCE (*J*_{SC} 16.7 mA/cm², *V*_{OC} 0.93 V, and FF 0.63), the TFB-based cell records a substantially higher efficiency (by 11%) due to the higher *J*_{SC}, *V*_{OC}, and FF. More explanations will be discussed below. The solar cell efficiency histograms of the HTMs based solar cells are shown in Figure S2 (Supporting Information) along with the Gaussian fitting. As a result, the average efficiency of the TFB based perovskite solar cells is about 9.68%, whereas the cells based on Spiro-OMeTAD only have 8.82% average efficiency. The average efficiency difference between TFB and Spiro-OMeTAD is 0.86%, which is close to the best performing cell efficiency difference of 1.14%.

Figure 4A presents the IPCE spectra of the solar cells, which correlate well with the corresponding *J*_{SC} values; the integrated photocurrent densities from the IPCE spectra are in fairly good

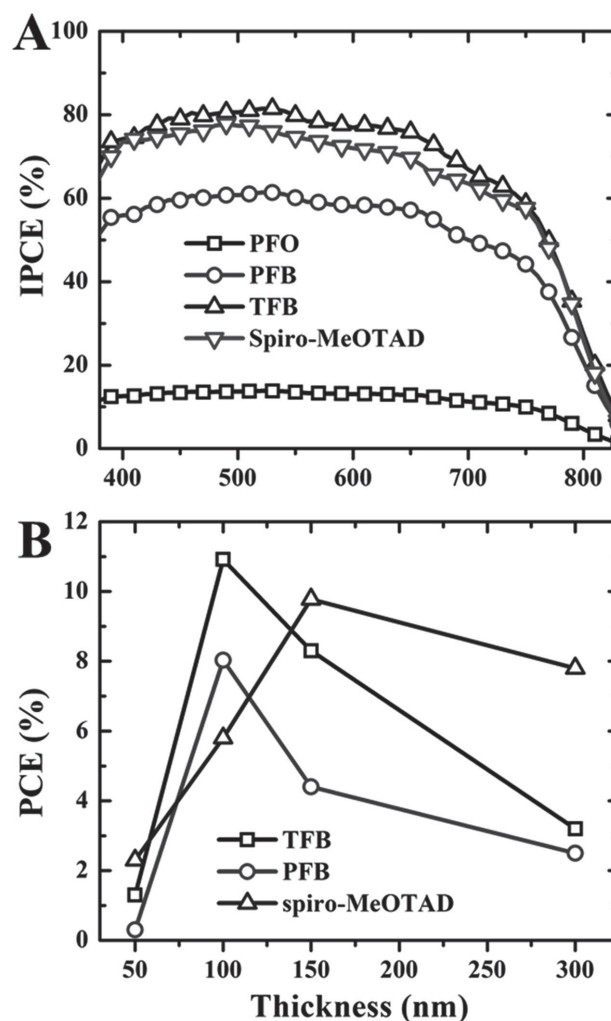


Figure 4. A) IPCE spectra of the perovskite solar cells, PFO (square line), PFB (circle line), TFB (up triangle line), Spiro-MeOTAD (down triangle line). B) Effects of the thickness of hole transport materials, which was obtained from SEM and surface profiler measurements, on PCE for different hole transport materials. TFB (square line), PFB (circle line), Spiro-MeOTAD (up triangle line).

agreement with the corresponding measured short-circuit photocurrents (see Figure S3, Supporting Information). To find the optimal HTL thickness for the related devices, we fabricated and investigated a series of solar cells with different thicknesses of PFB, TFB and spiro-OMeTAD (Figure 4B). It turns out that the maximum PCE for the polymer HTL occurs at a relatively thin thickness of ≈ 100 nm for TFB, which is to be compared to the over 150 nm thickness for spiro-OMeTAD. With the thickness increase of PFB and TFB, the PCE values is decreased. This could be explained by our morphology image in Figure S1 (Supporting Information), in which the TFB could cover well at 100 nm thickness. But when the thickness increases, the hole diffusion length in HTL would also prolong, so the transport resistance would also increase. Being different from spiro-OMeTAD's thick layer, a thinner thickness of TFB and PFB would achieve high performance.

It should be mentioned again that the extensive PV performance result from the two-step perovskite deposition is also presented in Supporting Information. As shown in Supporting Information Figure S5 and Table S3, the solar cells based on TFB reached a PCE of 12.80%, which is comparable to that with spiro-OMeTAD (13.58%). The average PCEs of solar cells based on TFB (11.72%) and spiro-OMeTAD (12.16%) are also close. Although the cell performance of the polymeric HTM is not higher than that of spiro-OMeTAD, the comparable cell performance still supports that the polymer is an excellent HTM for perovskite solar cells. Note that the PCEs of the solar cells fabricated by the two-step deposition method are higher than those by the one-step deposition method as reported previously,^[14] which could be ascribed to the submicrometer-sized $\text{CH}_3\text{NH}_3\text{PbI}_3$ crystals and the perfectly infiltrated PbI_2 into the TiO_2 mesoporous network.^[15]

2.4. Dynamic Photoluminescence Spectroscopy

Figure 5A shows steady state photoluminescence (PL) spectra of the TiO_2 /perovskite/HTL and TiO_2 /perovskite samples assembled on sapphire substrates. The HTL thickness was chosen at its best cell performance, so the TFB, PFO, and PFB layers are all about 100 nm thick, while the spiro-OMeTAD layer is about 200 nm thick. All of the samples exhibit a PL peak at 760 nm originated from the perovskite $\text{CH}_3\text{NH}_3\text{PbI}_3$. In this experiment, sapphire was used as the substrate because spin-coating coupled with heat treatment could deposit well-defined heterostructures on it without interpenetration. When a HTL is present, the perovskite PL quantum yield of perovskite/HTL film was largely reduced compared to the bare perovskite film. This PL quenching is attributed to the charge carrier extraction across the interface between $\text{CH}_3\text{NH}_3\text{PbI}_3$ and HTMs. However, the degree of PL varies depending on the identity of the HTL. Here we define the PL quenching efficiency by hole extraction to different HTMs as:^[30]

$$\eta_{\text{quench}} = \frac{\text{PL}_{\text{bare}} - \text{PL}_{\text{quench}}}{\text{PL}_{\text{quench}}} \quad (1)$$

where PL_{bare} and $\text{PL}_{\text{quench}}$ are integrated PL intensities of perovskite on sapphire substrates without and with the quenching

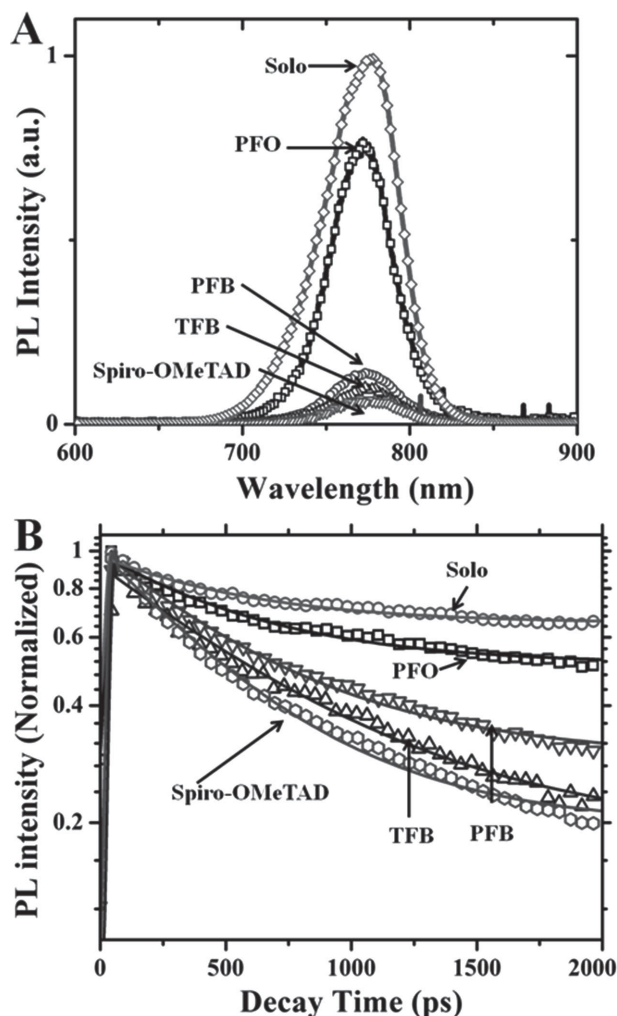


Figure 5. Steady-state photoluminescence (PL) spectra (A) and PL decay spectra (B) of PFO, PFB, TFB, spiro-OMeTAD on $\text{TiO}_2/\text{CH}_3\text{NH}_3\text{PbI}_3$ film and contrast film with solo $\text{TiO}_2/\text{CH}_3\text{NH}_3\text{PbI}_3$. Note the steady-state PL was excited at 514.5 nm (20 mW) and the PL decay were under the excitation wavelength 266 nm and the incident light intensity was 1 W/cm^2 .

HTM layer. We find that under the same measurement conditions, the PL quenching efficiency of the HTMs follows the orders of $\eta_{\text{PFO}} < \eta_{\text{PFB}} < \eta_{\text{TFB}} < \eta_{\text{spiro-OMeTAD}}$, the values of which are also tabulated in Table 1. The PFO layer quenches the perovskite PL by only less than 25%, whereas as much as 80–95% of the perovskite PL is quenched by the PFB, TFB, or spiro-OMeTAD layer. Here, higher mobilities would reduce the effects of space charge, and probably enhance the separation of electron-hole pairs immediately after exciton dissociation.^[31] That explains why TFB shows a higher quenching efficiency η_{PI} by virtue of the higher mobility. Spiro-OMeTAD also exhibits a sizable η_{PI} due to the charge mobility under photo-illumination.

To further study the charge transfer dynamics in the HTL, we had recourse to the time resolved photoluminescence (TrPL) spectroscopy. The TrPL traces were collected with the pump laser Ti:sapphire femtosecond-pulsed laser at 400 nm (3.1 eV). Although the accessible dynamic range is below 2 ns with this set-up, by which time the strongest quencher spiro-OMeTAD

Table 2. The parameters of device performance based on different HTMs by one-step $\text{CH}_3\text{NH}_3\text{PbI}_3$ deposition method on TiO_2 mesoporous perovskite solar cells.

HTMs used in devices	V_{OC} [V]	J_{SC} [mA/cm ²]	FF	PCE [%]	R_{S} [Ω cm ²]
PFO	0.61	3.6	0.56	1.22	13.6
PFB	0.91	13.8	0.64	8.03	9.4
TFB	0.96	17.5	0.65	10.92	7.5
spiro-OMeTAD	0.93	16.7	0.63	9.78	10.8

only quenched less than 80% of the perovskite PL, we could still find the PL quenching rate order of the perovskite/HTL films: spiro-OMeTAD > TFB > PFB > PFO. This agrees with the steady state PL measurement results. The TrPL data generally shows a non-monoexponential decay, so we fitted the lifetime of the perovskite/HTL films with a bi-exponential decay function below:

$$I(t) = A_1 \exp\left(-\frac{t}{\tau_1}\right) + A_2 \exp\left(-\frac{t}{\tau_2}\right) \quad (2)$$

The fitting parameters are summarized in Table S1 (Supporting Information). There was a bi-exponential fitting rather than monoexponential fitting because the initially photogenerated intrachain excitons start to migrate toward defects while relaxing toward lower energy states and that's why there was a smaller time constants τ_1 .^[32] The larger time constant τ_2 reflects the exciton lifetime of $\text{CH}_3\text{NH}_3\text{PbI}_3$. The order of τ_2 is $\tau_2(\text{spiro-OMeTAD}) < \tau_2(\text{TFB}) < \tau_2(\text{PFB}) < \tau_2(\text{PFO})$, so spiro-OMeTAD induces the fastest PL decay and TFB gives rise to the fastest PL decay among the three fluorine based polymers. From the results of steady-state PL and TrPL spectroscopies, TFB has the best charge separation ability among the three polymers. Although spiro-OMeTAD shows somewhat better charge separation ability than TFB, the difference is quite small.

2.5. Dynamic Impedance Spectroscopy

Electrochemical impedance spectroscopy (EIS) was used to measure charge transport parameters in the solar cells, such as chemical capacitance, recombination resistance, charge conductivity, and so forth. These parameters take important place in helping to explain the factors that determine the performance metrics of the HCPs in the corresponding solar cells, such as V_{OC} , FF, and J_{SC} . The FF is related to the series resistance (R_{S}), and the high performance solar cell should have a low R_{S} . Table 2 gives the values of R_{S} for different perovskite solar cells. For the same device structure but different HTLs, the R_{S} order is found to be $R_{\text{S}}(\text{TFB}) < R_{\text{S}}(\text{PFB}) < R_{\text{S}}(\text{spiro-OMeTAD}) < R_{\text{S}}(\text{PFO})$, which is in agreement with the order of FFs of the respective solar cells.

Figure 6 presents Nyquist plots of the solar cells with different HTLs, which were recorded at different applied voltages under 1-sun illumination. The frequency range for all of the EIS measurements is from 1 Hz to 1 MHz. The EIS spectra were fitted to an appropriate equivalent circuit model shown in Figure 6E. We applied a bias voltage ranging from 0 V to

0.6 V as transport in the high frequency region would meet very small resistance, making it difficult to model the exact transport resistance value. The Nyquist plots typically can be demarked into two main regions or arcs at high and low frequencies. We didn't find a clear transmission line (TL) under illumination. A TL feature is typically originated from the transport of electrons through a TiO_2 nanostructured network coupled to the recombination between electron sides (TiO_2) and hole sides (HTL). Here, similar to what was reported previously, the absence of TL behavior is likely due to the very thin TiO_2 films and the low electron transport resistance does not allow for the adequate resolution of any TL feature.

According to a previous report about $\text{CH}_3\text{NH}_3\text{PbI}_3$, we used a simplified circuit model (see Figure 6E)^[21,33] and assigned the arc at high frequencies to diffusion of holes through the transporting materials. For the sake of convenience, a parallel hole transport layer resistance (R_{HTL})–chemical capacitance (C_{HTL}) subcircuit was applied, where R_{HTL} and C_{HTL} represent the hole transport resistance and capacitance, respectively, thus combining the geometric capacitance and hole accumulation in the HTL. As there is no linear part (TL), the arc in the low frequency region is assigned to the recombination resistance R_{rec} and the parallel chemical capacitance C_{μ} .

An important factor on the solar cell performance is the recombination resistance (see data in Figure 7A). After the separation of photogenerated carriers, they can recombine before arriving to the selective extraction contacts, reducing the cell efficiency. So recombination is one of the main factors limiting the cell performance. Figure 7A shows a comparison of the recombination resistance of different HTMs. The IS data were recorded under illumination. R_{rec} is plotted against the applied bias voltage. Comparison of the four curves shows that the shunt resistance makes the R_{rec} flat down in the low potential region. Then R_{rec} followed an exponential decrease with increasing applied voltage. This exponential behavior is typical of a recombination resistance on TiO_2 based solar cell and also observed in other reports.^[21]

Figure 7A presents the comparison of recombination resistance (R_{rec}) of the different HTMs based perovskite solar cells. We find that at low applied voltage, the order of R_{rec} is $R_{\text{rec}}(\text{PFO}) > R_{\text{rec}}(\text{spiro-OMeTAD}) \sim R_{\text{rec}}(\text{PFB}) > R_{\text{rec}}(\text{TFB})$, while at high applied voltage, the corresponding R_{rec} order is $R_{\text{rec}}(\text{PFO}) > R_{\text{rec}}(\text{PFB}) \sim R_{\text{rec}}(\text{spiro-OMeTAD}) \sim R_{\text{rec}}(\text{TFB})$. The similar recombination resistance of PFB, spiro-OMeTAD, and TFB based perovskite solar cells indicate that the interfacial processes in both $\text{TiO}_2/\text{CH}_3\text{NH}_3\text{PbI}_3$ and $\text{CH}_3\text{NH}_3\text{PbI}_3/\text{HTM}$ as well as their energy losses are also similar. Therefore, taking into account that the contributions of recombination resistance

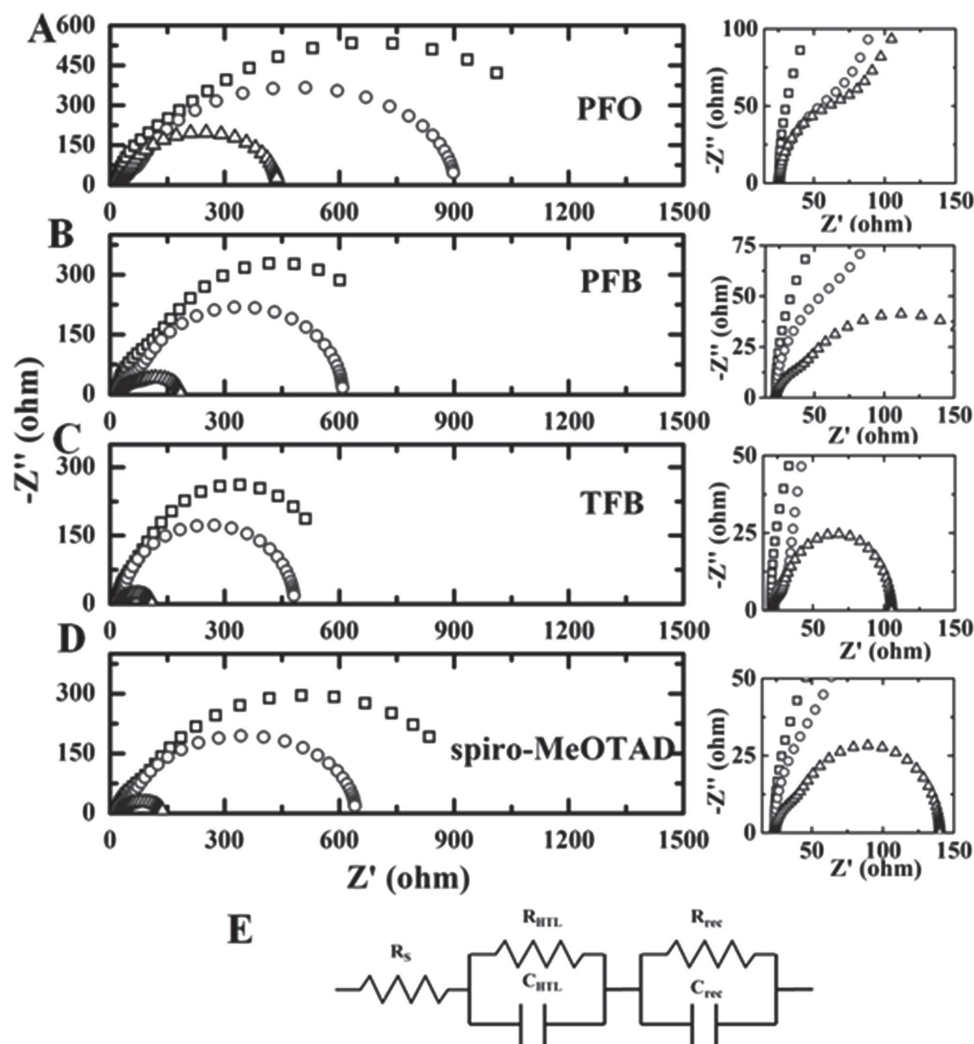


Figure 6. Impedance spectroscopy characterization. The representative Nyquist plots of whole (left) and high (right) frequency regions of impedance spectra at different biases (short-circuit 0 V (square line), 0.3 V (circle line), 0.6 V (up triangle line)) of $\text{TiO}_2/\text{CH}_3\text{NH}_3\text{PbI}_3/\text{HTL}$ solar cells under AM 1.5 G illumination at $100 \text{ mW}/\text{cm}^2$. The cells were employing different hole transport materials of A) PFO, B) PFB, C) TFB, and D) spiro-MeOTAD. E) The equivalent circuit used for fitting the Nyquist plots.

of PFB, TFB and spiro-OmeTAD on the V_{OC} values are similar, we can conclude that the differences in their V_{OC} , for example, $V_{\text{OC}}(\text{TFB}) > V_{\text{OC}}(\text{spiro-OmeTAD}) \sim V_{\text{OC}}(\text{PFB})$, can be attributed to their different HOMO levels of HTL in the order of $E_{\text{HOMO}}(\text{TFB}) < E_{\text{HOMO}}(\text{spiro-OmeTAD}) \sim E_{\text{HOMO}}(\text{PFB})$. This is reasonable since V_{OC} is determined by the difference of conduction band of TiO_2 and the HOMO level of HTMs.^[6,34]

We extracted and analyzed the parameters from the fitted impedance spectra in the high frequency region. The resulting hole conductivity of HTL, σ_{HTL} , is derived from R_{HTL} according to

$$R_{\text{HTL}} = \frac{L}{A\sigma_{\text{HTL}}} \quad (3)$$

where A is active film of area and L is the thickness.^[35] The obtained values σ_{HTL} are plotted versus applied bias in Figure 7B. The hole conductivity in each cell is generally

increased when the applied voltage increases, due to the higher hole density in HTL as a consequence of hole injection from perovskite into HTL.^[35b] On comparing these four polymers, we find that the order of electrical conductivities are $\sigma_{\text{TFB}} > \sigma_{\text{spiro-OmeTAD}} > \sigma_{\text{PFB}} > \sigma_{\text{PFO}}$. This sequence is in agreement with the data in Table 1 published in the literature. The higher hole conductivity leads to a lower voltage loss and higher fill factor of TFB than spiro-OmeTAD as we have observed. We further tested the hole injection characteristics of hole-only devices by the structure ITO/interlayer/HTM/Au in Figure S4 (Supporting Information).^[36] The hole-injection fluence of the devices based on PFB, TFB, and spiro-OmeTAD is much greater than that of the PFO device. The hole-injection capacity follows the order of $\text{TFB} > \text{PFB} > \text{spiro-OmeTAD} > \text{PFO}$, which is similar to the results of electrical conductance obtained from the impedance spectra (IS).

Therefore, the impedance spectra above provide some information about the carrier transport and recombination, which

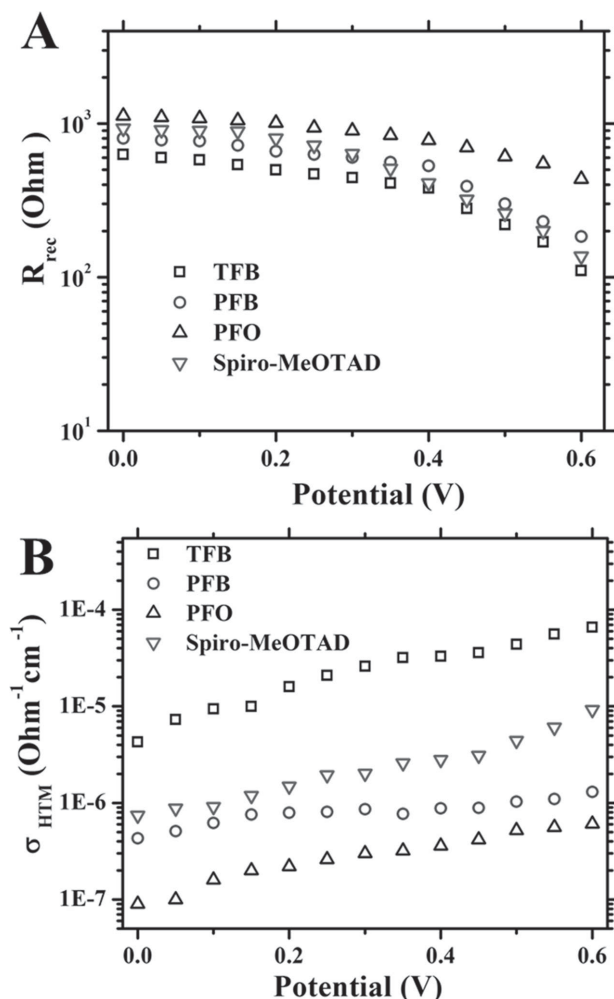


Figure 7. Series of characteristic recombination resistance R_{rec} (A) and hole transport materials conductivity σ_{HTM} (B) from impedance spectroscopy measurements obtained from the cells at different bias voltage under 1 sun illumination. PFO (up triangle line), PFB (circle line), TFB (square line), spiro-MeOTAD (down triangle line).

help us to understand the process of charge transfer, especially at the interface between perovskite and HTL. The lower recombination rate and higher hole conductivity of TFB than spiro-OMeTAD support the better performance of TFB-based solar cells.

3. Conclusion

We have systematically investigated a series of fluorene derived polymer materials (PFB, TFB and PFO) for the HTL in perovskite solar cells fabricated primarily under the one-step perovskite deposition condition. All of the three HCPs showed reasonably good performance, but TFB is found to be the best performing HCP for perovskite solar cells with PCEs reaching up to 10.92%, even higher than the spiro-OMeTAD based cells. Photoluminescence study shows the highest hole extraction rate of TFB. The impedance spectroscopy study reveals the higher hole conductivity and lower series resistance of TFB

than spiro-OMeTAD, which could explain the higher fill factor, short-circuit photocurrent and open-circuit voltage of the corresponding solar cells. With the two-step perovskite deposition method, we were able to achieve about 13% efficient solar cells for TFB (12.80%) and spiro-OMeTAD (13.58%), again establishing that TFB is a potential contender for polymeric HTM in perovskite solar cells. Our systematic results will expedite the design of new HTMs, especially the design of high efficiency and low cost HTMs, for hybrid solar cells.

4. Experimental Section

Materials Synthesis and Preparation: Unless stated otherwise, all materials were purchased from Sigma-Aldrich or J&K. PFO Mw = 50 000–150 000 (GPC) and TFB Mw > 30 000 (GPC) are commercialized and could be purchased from Luminescence Technology Corporation and PFB (Mw = 20 000–150 000) is from American Dye Source, Inc. Spiro-MeOTAD (99%) was purchased from Derthon Optoelectronic Materials Science & Technology Co., Ltd. $\text{CH}_3\text{NH}_3\text{I}$ was synthesized according to a reported procedure. For a typical synthesis, 0.3 mol (38 mL) methylamine CH_3NH_2 solution (33 wt% in absolute ethanol) was reacted with equimolar (40 mL) hydroiodic acid (HI) (57 wt% in water) with stirring at ice bath for about 2 h to synthesis methylammonium iodide ($\text{CH}_3\text{NH}_3\text{I}$). Crystallization of $\text{CH}_3\text{NH}_3\text{I}$ was achieved using a rotary evaporator at 60 °C for 2–3 h. The obtained $\text{CH}_3\text{NH}_3\text{I}$ power with equimolar lead(II) iodide (PbI_2) were dissolved in γ -butyrolactone with stirring at 60 °C for over-night to produce a 2.5 mM $\text{CH}_3\text{NH}_3\text{PbI}_3$ precursor solution.

Solar Cell Fabrication: First, fluorine doped tin oxide (F:SnO_2) coated glass (FTO) was patterned by laser etching. The patterned FTO were cleaned by ultrasonication and rinsed in the deionized water and mixed solution ethanol and acetone (v:v = 1:1). An 30–40 nm thick TiO_2 compact layer was then deposited on the substrates by aerosol spray pyrolysis at 50 mm titanium diisopropoxide bis(acetylacetonate) solution (75% in 2-propanol), diluted in ethanol. The nanocrystalline TiO_2 paste was deposited by screen-printed method and calcined at 500 °C for 1 h. The films then immersed in 40 mM of TiCl_4 aqueous solution at 60 °C for 1 h and heat-treated at 500 °C for 30 min. For one-step $\text{CH}_3\text{NH}_3\text{PbI}_3$ deposition method, the $\text{CH}_3\text{NH}_3\text{PbI}_3$ solution prepared above was deposited onto the TiO_2 meso-structure by spin-coating at 3000 r.p.m. for 60 s, and dried on a hot plate at 100 °C for 20 min. For two-step $\text{CH}_3\text{NH}_3\text{PbI}_3$ deposition method, PbI_2 (450 mg/mL) in N,N -dimethylformamide (DMF) was spin-coated onto the the TiO_2 meso-structure, which was then dipped in a solution of $\text{CH}_3\text{NH}_3\text{I}$ in 2-propanol (10 mg/mL) for 20 s and rinsed with 2-propanol. The resulting film was dried at room temperature for 3 min and then on a hot plate at 100 °C for 10 min. The hole transport material (HTM) was deposited on the $\text{CH}_3\text{NH}_3\text{PbI}_3/\text{TiO}_2$ meso-structure film by spin coating at 3000 r.p.m. for 30 s. The HTM solution was prepared by dissolving HCPs in chlorobenzene (25 mg/1 mL), 26 μL tert-butylpyridine (TBP) solution and 35 μL Li-bis(trifluoromethanesulfonyl) imide (Li-TFSI)/acetonitrile (170 mg/1 mL). The spiro-OMeTAD solution was prepared with a concentration of 80 mg/mL in chlorobenzene, into which 28 μL TBP and 35 μL Li-TFSI/acetonitrile (520 mg/1 mL) were added. For the metal electrode, 60 nm thickness of gold was deposited on the top of the HTM by a thermal evaporation through a metal shadow mask to define the active area of the devices ($\approx 12.8 \text{ mm}^2$) and to form a top anode. The cell was packaged by scribbling UV-glue on the top and covered a glass slides, then the cell was exposed to UV light radiation for 10 min to make the glue solidify. The device testing was carried out the glove box after packaging and tested within a metal mask of an aperture (7 mm² area).

Characterization: The light source (Oriel solar simulator, 450 W Xe lamp, AM 1.5 global filter) was calibrated to 1 sun (100 mW/cm²) using an optical power meter (Newport, model 1916-C) equipped with a Newport 818P thermopile detector. J - V characteristic curves were

measured by the Zahner controlled intensity modulated photoresponse spectroscopy (C-IMPS) system. We measured the EIS spectra at an applied bias of Voc and a frequency range from 1 Hz and 1 MHz with AC amplitude of 10 mA under illumination of simulated solar AM1.5 global light at 100 mW/cm². Z-View Analyst software was used to model the Nyquist plots obtained from the impedance measurements. Incident photon to current conversion efficiencies (IPCEs) was measured on photo current spectra system of CIMPS (CIMPS-PCS) with tunable light source (TLS03). Morphologies of the nanomaterials and subsequent nanostructures were directly examined on JEOL6700F SEM at an accelerating voltage of 5 kV. Absorption spectra were carried out on the same film samples using a Perkin-Elmer UV-vis spectrophotometer (model Lambda 20). The film thickness was determined by a Tencor Alpha-Step 200 surface profiler system. Steady-State Photoluminescence were conducted with a Renishaw 2000 laser Raman microscope equipped with a 514.5 nm 20 mW argon ion laser of 2 mm spot size for excitation. For TrPL measurements, a tunable Ti:sapphire femtosecond-pulsed laser was used as the excitation light source, with the excitation wavelength 400 nm and the incident light intensity was 1 W cm⁻². A Hamamatsu C5680-04 streak camera was used for TrPL. For mobility measurement, the hole injecting layer of HTM was deposited onto a pre-etched indium tin oxide substrate by spin-coating. A gold back electrode was then deposited by thermal evaporation. *I*-*V* curves were measured using a computer-controlled Keithley 2400 sourcemeter.

Supporting Information

Supporting Information is available from the Wiley Online Library or from the author.

Acknowledgements

This work was supported by the HK-RGC General Research Funds (HKUST 606511 and 605710).

Received: May 14, 2014

Revised: August 17, 2014

Published online:

- [1] a) D. G. Nocera, *Inorg. Chem.* **2009**, *48*, 10001; b) S. Chu, A. Majumdar, *Nature* **2012**, *488*, 294.
- [2] a) A. Goetzberger, C. Hebling, H. W. Schock, *Mater. Sci. Eng. R* **2003**, *40*, 1; b) A. Shah, P. Torres, R. Tscharnner, N. Wyrsh, H. Keppner, *Science* **1999**, *285*, 692.
- [3] R. B. Bergmann, *Appl. Phys. A* **1999**, *69*, 187.
- [4] H. W. Schock, *Appl. Surf. Sci.* **1996**, *92*, 606.
- [5] J. Y. Kim, K. Lee, N. E. Coates, D. Moses, T. Q. Nguyen, M. Dante, A. J. Heeger, *Science* **2007**, *317*, 222.
- [6] A. J. Nozik, M. C. Beard, J. M. Luther, M. Law, R. J. Ellingson, J. C. Johnson, *Chem. Rev.* **2010**, *110*, 6873.
- [7] a) V. I. Klimov, *J. Phys. Chem. B* **2006**, *110*, 16827; b) J. A. McGuire, J. Joo, J. M. Pietryga, R. D. Schaller, V. I. Klimov, *Acc. Chem. Res.* **2008**, *41*, 1810.
- [8] N. Lopez, L. A. Reichertz, K. M. Yu, K. Campman, W. Walukiewicz, *Phys. Rev. Lett.* **2011**, *106*.
- [9] D. Kraemer, B. Poudel, H. P. Feng, J. C. Caylor, B. Yu, X. Yan, Y. Ma, X. W. Wang, D. Z. Wang, A. Muto, K. McEnaney, M. Chiesa, Z. F. Ren, G. Chen, *Nat. Mater.* **2011**, *10*, 532.
- [10] a) N. G. Park, *J. Phys. Chem. Lett.* **2013**, *4*, 2423; b) H. J. Snaith, *J. Phys. Chem. Lett.* **2013**, *4*, 3623.
- [11] A. Kojima, K. Teshima, Y. Shirai, T. Miyasaka, *J. Am. Chem. Soc.* **2009**, *131*, 6050.
- [12] J.-H. Im, C.-R. Lee, J.-W. Lee, S.-W. Park, N.-G. Park, *Nanoscale* **2011**, *3*, 4088.
- [13] a) M. M. Lee, J. Teuscher, T. Miyasaka, T. N. Murakami, H. J. Snaith, *Science* **2012**, *338*, 643; b) M. Z. Liu, M. B. Johnston, H. J. Snaith, *Nature* **2013**, *501*, 395.
- [14] J. Burschka, N. Pellet, S. J. Moon, R. Humphry-Baker, P. Gao, M. K. Nazeeruddin, M. Gratzel, *Nature* **2013**, *499*, 316.
- [15] a) H. S. Kim, S.-H. Im, N.-G. Park, *J. Phys. Chem. C* **2014**, *118*, 5615; b) J.-W. Lee, T.-Y. Lee, P. J. Yoo, M. Gratzel, S. Mhaisalkar, N.-G. Park, *J. Mater. Chem. A* **2014**, *2*, 9251.
- [16] Z. Zhu, J. Ma, Z. Wang, C. Mu, Z. Fan, L. Du, Y. Bai, L. Fan, H. Yan, D. L. Phillips, S. Yang, *J. Am. Chem. Soc.* **2014**, *136*, 3760.
- [17] H. J. Snaith, M. Gratzel, *Phys. Chem. Lett.* **2007**, *98*, 177402.
- [18] a) H. J. Snaith, M. Graetzel, *Appl. Phys. Lett.* **2006**, *89*, 262114; b) H. J. Snaith, L. Schmidt-Mende, *Adv. Mater.* **2007**, *19*, 3187; c) J. Burschka, A. Dualeh, F. Kessler, E. Baranoff, N.-L. Cevey-Ha, C. Yi, M. K. Nazeeruddin, M. Graetzel, *J. Am. Chem. Soc.* **2011**, *133*, 18042.
- [19] N. J. Jeon, J. Lee, J. H. Noh, M. K. Nazeeruddin, M. Gratzel, S. I. Seok, *J. Am. Chem. Soc.* **2013**, *135*, 19087.
- [20] H. Li, K. Fu, A. Hagfeldt, M. Grätzel, S. G. Mhaisalkar, A. C. Grimsdale, *Angew. Chem. Int. Ed.* **2014**, *53*, 4085.
- [21] J. A. Christians, R. C. M. Fung, P. V. Kamat, *J. Am. Chem. Soc.* **2013**, *136*, 758.
- [22] a) N. J. Jeon, J. H. Noh, Y. C. Kim, W. S. Yang, S. Ryu, S. I. Seok, *Nat. Mater.* **2014**, *13*, 897; b) J. H. Heo, S. H. Im, J. H. Noh, T. N. Mandal, C. S. Lim, J. A. Chang, Y. H. Lee, H. J. Kim, A. Sarkar, M. K. Nazeeruddin, M. Gratzel, S. I. Seok, *Nat. Photonics* **2013**, *7*, 487.
- [23] a) O. Malinkiewicz, A. Yella, Y. H. Lee, G. M. Espallargas, M. Graetzel, M. K. Nazeeruddin, H. J. Bolink, *Nat. Photonics* **2014**, *8*, 128; b) B. Conings, L. Baeten, C. D. Dobbelaere, J. D. Haen, J. Manca, H. G. Boyen, *Adv. Mater.* **2014**, *26*, 2041.
- [24] C. Li, M. Y. Liu, N. G. Pschirer, M. Baumgarten, K. Mullen, *Chem. Rev.* **2010**, *110*, 6817.
- [25] D. Poplavskyy, J. Nelson, D. D. C. Bradley, *Appl. Phys. Lett.* **2003**, *83*, 707.
- [26] A. Buckley, D. Pickup, C. Yates, Y. Zhao, D. Lidzey, *J. Appl. Phys.* **2011**, *109*.
- [27] H. H. Fong, A. Papadimitratos, J. Hwang, A. Kahn, G. G. Malliaras, *Adv. Funct. Mater.* **2009**, *19*, 304.
- [28] a) H. T. Nicolai, G. A. H. Wetzelaer, M. Kuik, A. J. Kronemeijer, B. de Boer, P. W. M. Blom, *Appl. Phys. Lett.* **2010**, *96*, 172107; b) D. Poplavskyy, J. Nelson, D. D. C. Bradley, *Macromol. Symp.* **2004**, *212*, 415.
- [29] a) J. H. Heo, S. H. Im, J. H. Noh, T. N. Mandal, C.-S. Lim, J. A. Chang, Y. H. Lee, H.-j. Kim, A. Sarkar, M. K. Nazeeruddin, M. Graetzel, S. I. Seok, *Nat. Photonics* **2013**, *7*, 487; b) H.-S. Kim, C.-R. Lee, J.-H. Im, K.-B. Lee, T. Moehl, A. Marchioro, S.-J. Moon, R. Humphry-Baker, J.-H. Yum, J. E. Moser, M. Graetzel, N.-G. Park, *Sci. Rep.* **2012**, *2*, 591.
- [30] S. R. Scully, P. B. Armstrong, C. Edder, J. M. J. Frechet, M. D. McGehee, *Adv. Mater.* **2007**, *19*, 2961.
- [31] a) V. D. Mihailetchi, J. Wildeman, P. W. M. Blom, *Phys. Chem. Lett.* **2005**, *94*, 126602; b) V. D. Mihailetchi, L. J. A. Koster, J. C. Hummelen, P. W. M. Blom, *Phys. Chem. Lett.* **2004**, *93*, 216601.
- [32] D. E. Markov, J. C. Hummelen, P. W. M. Blom, A. B. Sieval, *Phys. Rev. B* **2005**, *72*, 045216.
- [33] P. P. Boix, G. Larramona, A. Jacob, B. Delatouche, I. Mora-Sero, J. Bisquert, *J. Phys. Chem. C* **2012**, *116*, 1579.
- [34] A. Hagfeldt, G. Boschloo, L. C. Sun, L. Kloo, H. Pettersson, *Chem. Rev.* **2010**, *110*, 6595.
- [35] a) V. Gonzalez-Pedro, E. J. Juarez-Perez, W.-S. Arsyad, E. M. Barea, F. Fabregat-Santiago, I. Mora-Sero, J. Bisquert, *Nano Lett.* **2014**, *14*, 888; b) F. Fabregat-Santiago, G. Garcia-Belmonte, I. Mora-Sero, J. Bisquert, *Phys. Chem. Chem. Phys.* **2011**, *13*, 9083.
- [36] J. Cui, Q. L. Huang, J. G. C. Veinot, H. Yan, T. J. Marks, *Adv. Mater.* **2002**, *14*, 565.